Journal of Materials Chemistry C

ROYAL SOCIETY OF CHEMISTRY

PAPER

View Article Online
View Journal | View Issue

Cite this: J. Mater. Chem. C, 2025, 13, 1228

Facile synthesis of silicon quantum dots with photoluminescence in the near-ultraviolet to violet region *via* wet oxidation†

Yizhou He,[a] Qianxi Hao,[a] Chi Zhang,[a] Qi Wang,[a] Wenxin Zeng,[a] Jiamin Yu,[b] Xue Yang,*[b] Shaorong Li,[a] Xiaowei Guo *[ac] and Serguei K. Lazarouk[d]

Received 21st May 2024,
Accepted 5th November 2024

DOI: 10.1039/d4tc02095b

rsc.li/materials-c

To extend the photoluminescence (PL) of silicon quantum dots (SiQDs) into the near-ultraviolet–violet (NUVV) region, the size of SiQDs must be reduced to less than 1.53 nm. However, this significantly increases both the difficulty and the cost of synthesis. Herein, we report a facile wet oxidation treatment to obtain SiQDs with PL emission in the NUVV region while elucidating their emission mechanism. The synthesized SiQDs exhibit an average diameter of 4.95 nm, with F-band emission peaks ranging from 332 to 420 nm, which are blue-shifted by approximately 500 nm compared to the near-infrared (NIR) counterparts lacking wet oxidation treatment. Notably, the synthesized SiQDs achieve an average photoluminescence quantum yield (PLQY) of 19.05%, a 6.24-fold increase over their NIR counterparts. Comprehensive examinations attribute this NUVV emission to two types of oxygen defects: peroxy linkage (POL) and oxygen-deficient center (ODC(I)). Under wet oxidation conditions, SiO_x networks containing these oxygen defects, rather than simple Si–O–Si groups, are formed on the surface of SiQDs. Furthermore, after storing the SiQDs in ambient air for approximately two months, no intrinsic or additional defect-induced emissions were observed, and 88% of the initial PLQY was retained, indicating favorable stability of the SiQDs. This study provides valuable insights into oxygen-related defect-induced emission mechanisms on SiQD surfaces.

1. Introduction

Thanks to the abundance and environmentally benign properties of silicon, silicon quantum dots (SiQDs) are expected to serve as alternatives to rare earth phosphors and II–VI semiconductor QDs luminescent materials, thus contributing to the advancement of the sustainable development goals (SDGs).[1] Various methods have been developed for synthesizing SiQDs to date, including pulsed laser ablation of solid silicon,[2–7] electrochemical etching of silicon wafers,[8–10] reduction of halosilanes,[11–15] solution synthesis,[16,17] plasma synthesis,[18–20] thermal pyrolysis of hydrogen silsesquioxane (HSQ) or HSQ polymers,[1,21–49] and other unconventional techniques.[50–52] Among these methods, thermal pyrolysis is particularly advantageous due to its low equipment requirements and the high quality of synthesized SiQDs.[1,30] To enable the utilization of SiQDs in light-emitting devices (LEDs),[53–59] photodetectors,[60,61] biomedical imaging,[43,44] photovoltaics,[62,63] and other applications,[64] it is essential to achieve emission that spans the entire visible spectrum. The quantum confinement effect allows for the precise control of the size of SiQDs between 2 and 10 nm, resulting in red, orange, and yellow slow-band (S-band) photoluminescence (PL).[65,66] Furthermore, achieving S-band green, blue, and violet PL requires SiQDs with sizes smaller than 2 nm, 1.70 nm, and 1.53 nm, respectively, as predicted by the effective mass approximation (EMA) method.[66,67] However, this introduces significant challenges in terms of manufacturing complexity and costs, particularly for violet-blue-emitting SiQDs.[67,68] Moreover, literature reports indicate that even with SiQDs sized between 1 and 1.6 nm, violet-blue emission remains difficult to achieve.[69]

Surface engineering has emerged as a promising approach for producing blue-emitting SiQDs, where the fast-band (F-band) violet-blue PL primarily arise from surface effects rather than size-related quantum confinement.[65,67] Various ligands, such as siloxane, nitrogen species, halogens, acetal, and amine, have

[a] School of Optoelectronic Science and Engineering, University of Electronic Science and Technology of China, Chengdu 610054, China. E-mail: gxw@uestc.edu.cn
[b] China National Tobacco Corporation Sichuan Company, Chengdu, 610041, China. E-mail: 280055419@qq.com
[c] Yangtze Delta Region Institute (Huzhou), University of Electronic Science and Technology of China, Huzhou 313001, China
[d] Belarusian State University of Informatics and Radioelectronics, P. Browka 6, Minsk 220013, Belarus

† Electronic supplementary information (ESI) available. See DOI: https://doi.org/10.1039/d4tc02095b

been shown to induce violet-blue emission from SiQDs.[24,40,70–72] Siloxane, functioning as a silica oxide ligand, can be generated *in situ* without additional reagents, thereby streamlining the synthesis process.[40,72–75] In 2010, de Boer *et al.* identified a violet-blue component (420 nm) within the PL spectra of SiQDs and attributed it to oxygen-related defects on the SiQD surface.[73] In 2011, Gupta *et al.* observed a shift in the PL of as-prepared hydride SiQDs (H-SiQDs) from orange (620 nm) to violet-blue (450 nm) following a single day of air exposure.[74] At approximately the same time, Yang *et al.* employed laser ablation to synthesize silicon nanoparticles (Si NPs) exhibiting a strong violet-blue emission (415–435 nm).[76] By monitoring the PL evolution of Si NPs during various treatments, they attributed this blue emission to the transfer of excitons generated in the Si NPs to near-interface traps (NITs) and their subsequent radiative recombination within the NITs. In 2013, Chiu *et al.* demonstrated a complete transition in the PL of cetyltrimethylammonium bromide/decane-passivated SiQDs (CTAB/Dec-SiQDs) from red (580 nm) to violet-blue (488 nm) after exposure to an alkaline environment (pH = 13.3) for three days.[75] In 2015, DeBenedetti *et al.* proposed that the conversion of the red PL (~580 nm) to the violet-blue PL (~450 nm) of Dec-SiQDs originated from the passivation of dangling bond defects by small alcohol molecules.[40] In 2022, Fujimoto *et al.* synthesized siloxane-passivated SiQDs, exhibiting violet-blue emission (400 nm) with a photoluminescence quantum yield (PLQY) of 12% *via* the $SiCl_4$ reduction method.[72] In 2024, Jingu *et al.* synthesized SiQDs exhibiting green PL at 530 nm by reducing $SiBr_4$ followed by ligand exchange with a carbazole derivative.[77] They stored the SiQDs in O_2-saturated ethanol and observed the emergence of violet-blue (470–480 nm) and yellow-green (540 nm) PL bands, which were attributed to SiO_x and alkoxy groups. Despite the significant efforts to produce SiQDs with violet-blue emissions associated with silicon oxides,[40,72–77] reports on emission peaks in the front part of the violet region (380–400 nm) and the near-ultraviolet region (NUV) (200–380 nm) remain scarce. Moreover, the highest PLQY achieved for these SiQDs is 12%,[40,72–77] substantially lower than the required PLQY for applications in LEDs, displays, and photovoltaics, which limits their practical applications.[65,67]

We propose a straightforward wet oxidation treatment to synthesize SiQDs exhibiting PL in the NUV-violet (NUVV) region and elucidate their emission mechanism. The synthesized SiQDs have a diameter of 4.95 nm and exhibit F-band emission peaks ranging from 332 to 420 nm. This range of PL peaks is blue-shifted by approximately 500 nm compared to the PL peaks of the untreated sample. Notably, the average PLQY of the NUVV-emitting SiQDs is 19.05%, representing a 6.24-fold increase over that of the untreated sample. Through characterization techniques including PL, transmission electron microscopy (TEM), X-ray diffraction (XRD), Raman spectroscopy, Fourier-transform infrared spectroscopy (FTIR), and electron paramagnetic resonance (EPR), we reveal that the NUVV emission originates from two types of oxygen-related defects in SiO_x and provide a comprehensive understanding of both the wet oxidation process and the mechanism of NUVV emission. Finally, after storing the NUVV-emitting SiQDs in ambient air for two months, we found that the stored sample retained 88% of its initial PLQY, indicating that SiQDs exhibit favorable air stability.

2. Experimental section

2.1. Materials

The following chemical reagents were used: triethoxysilane (Macklin, 97%), hydrochloric acid (Keshi, 37%), hydrofluoric acid (HF, Macklin, 48%), ethanol (Keshi, 99.7%), 1-octadecene (Macklin, 95%), mesitylene (Macklin, 97%), and toluene (Keshi, 99.5%).

2.2. Synthesis of NIR-emitting and NUVV-emitting SiQDs

We refer to the final near-infrared (NIR)-emitting and NUVV-emitting samples as NIR-QDs and NUVV-QDs. As shown in Fig. 1, the synthesis involved four sequential steps: hydrolysis–condensation, thermal pyrolysis, HF etching, and hydrosilylation.[1] All procedures were conducted in an argon glove box, except for the drying process following HF etching, which was likely carried out in ambient air.

(1) Hydrolysis–condensation: 30 mL of TES was combined with 15 mL of aqueous HCl (pH = 3) and then stirred magnetically for 5 to 10 minutes, resulting in a transparent gel-like substance. This substance was allowed to dry at room temperature for 96 hours to yield a dry HSQ polymer. It is important to clarify that a pH of 3 refers to the pH of the aqueous HCl solution prior to the addition and does not pertain to the overall pH after the addition.

(2) Thermal pyrolysis: the HSQ polymer was heated in a tube furnace under a carrier gas mixture of 5% hydrogen and 95% argon to 1000 °C and maintained for 6 hours. The heating rate and duration of each temperature step are provided in Table S1 and Fig. S1. A pyrolysis temperature of 1000 °C and the plateau temperature of 600 °C were adopted based on the literature.[30] It is important to note that the pyrolysis temperature of 1000 °C, which is lower than the conventional temperature of 1100 °C, is designed to be used in conjunction with a platform temperature of 600 °C to produce medium-sized SiQDs. The resulting black particles were ground into a fine brown powder.

(3) HF etching: It is important to emphasize that HF used in this process is extremely corrosive and, more importantly, poses a significant and potentially fatal hazard to human health. As a result, strict safety measures must be taken when working with HF. 300 mg of the powder, along with 16 mL of HF and 8 mL of ethanol, were added to a polytetrafluoroethylene (PTFE) bottle and stirred magnetically for 60 minutes. The resulting yellow solution was centrifuged at 12 000 rpm for 10 minutes, after which the supernatant was decanted to obtain the precipitate. This centrifugation step was repeated once more after adding ethanol. The precipitate was transferred to a Petri dish, and 6 mL of fresh ethanol was added. It was then dried under either argon or ambient air for 24 hours to obtain the hydrogen-passivated SiQD powder, corresponding to the final products, NIR-QDs and NUVV-QDs.

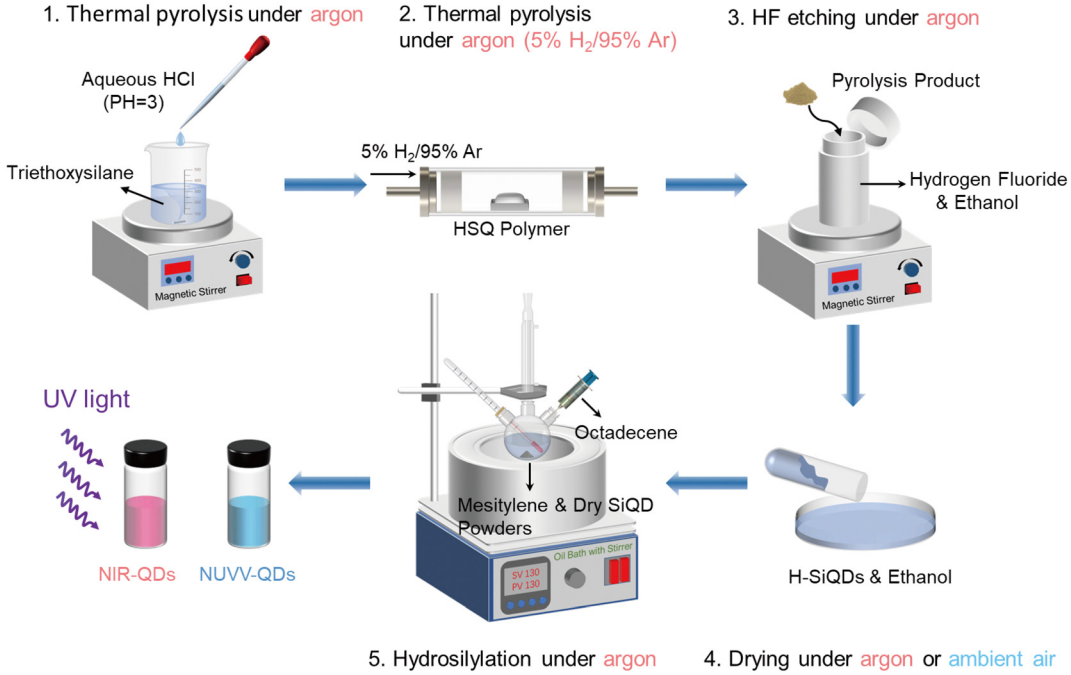

Fig. 1 A schematic diagram of the synthesis routes for NIR-emitting and NUVV-emitting SiQDs.

(4) Hydrosilylation: 30 mg of the hydrogen-passivated SiQD powder, along with 18 mL of 1-octadecene and 18 mL of mesitylene, were added to a triple-necked flask and heated in an oil bath at 130 °C for 20 hours. After cooling the solution to room temperature, 30 mL of ethanol was added, followed by centrifugation at 12 000 rpm for 20 minutes. If the earlier drying treatment atmosphere was argon, the supernatant was removed, and the precipitate was retained; then it was dried for 24 hours and dispersed in toluene, resulting in NIR-QDs. Conversely, if the drying atmosphere was ambient air, the supernatant was collected, resulting in NUVV-QDs.

Before characterizing the NUVV-QDs, the solution was transferred to a Petri dish and heated at 110 °C for 30 hours to ensure the removal of 1-octadecene and mesitylene. The dried NUVV-QDs were then dispersed in toluene for further characterization. This step was undertaken to replace the original solvent used with toluene.

2.3. Storage of NUVV-QDs in ambient air

A fresh solution of NUVV-QDs (with a solvent mixture of 1-octadecene, mesitylene, and ethanol) was transferred to a sample vial and removed from the glove box to be exposed to ambient air (15–25 °C, 30–55% RH) for 54 days. Subsequently, the sample was returned to the glove box, where it was poured into Petri dishes and heated at 110 °C for 30 hours to ensure the removal of 1-octadecene and mesitylene. The resulting dried NUVV-QDs were then dispersed in toluene for subsequent characterization of the PL spectra.

2.4. Characterization

Utilizing a Talos F200S G2 TEM (Thermo Fisher Scientific) at an operational acceleration voltage of 200 kV, measurements encompassing TEM, high-resolution TEM (HR-TEM), and selected area electron diffraction (SAED) were accomplished. XRD patterns were obtained using an Ultima IV diffractometer (Rigaku), utilizing CuKa radiation at a scanning rate of 5° min^{-1}. Raman scattering measurements were performed using a DXR3 Raman spectrometer (Thermo Scientific) equipped with a confocal microscope. The excitation wavelength and spectral resolution of Raman scattering spectra were 532 nm and 0.4821 cm^{-1}, respectively. The diameter of the laser spot was 2 microns, the laser power was 1.5 mW and the integration time was 30 s. FTIR spectroscopy was carried out with the aid of a Nicolet Is5 spectrometer (Thermo Fisher Scientific), employing an attenuated total reflection (ATR) module and achieving a resolution of 0.48 cm^{-1}. Before the FTIR measurement, the samples were subjected to heating at 70 °C for 10 hours to remove residual toluene. The resultant gel-like samples were then placed on a diamond ATR prism for testing. EPR experiments were performed using an A300 EPR spectrometer (Bruker) in the x-band, with a magnetic field sweep from B = 3460 to 3560 G. To quantify the surface dangling bond density of SiQDs, an ethanol solution of 2,2-diphenyl-1-picrylhydrazyl (DPPH) at a concentration of 1.0×10^{-3} mol L^{-1} was employed as the standard sample. A toluene solution of SiQDs with a concentration of 2 mg mL^{-1} served as the test sample. The volume of both DPPH and SiQDs solutions used for the measurement was 80 μL. Ultraviolet and visible absorption spectra (UV-Vis) were captured using a UV 3600 spectrophotometer (Shimadzu) with an integrating sphere. The PL spectra and PLQYs were determined using a Fluorolog-3 spectrofluorometer (Horiba Scientific) equipped with an IS80 integrating sphere (Labsphere) and a 450 W xenon lamp for excitation (λ_{ex} = 330 nm for the PLQY measurement), with a

CCD (SYNAPSE) serving as the detection mechanism. For the measurement of PL decay, the same Fluorolog-3 spectrofluorometer was employed, and this time using a DeltaDiode (317 nm, DD-320) for excitation and a picosecond photon detection module (PPD-850) to capture emissions (λ_{ex} = 355 nm, λ_{em} = 750 nm for NIR-QDs; λ_{ex} = 317 nm, λ_{em} = 350 nm for NUVV-QDs).

3. Results and discussion

3.1. PL analysis of SiQDs

Fig. 2(a) and (d) present the two-dimensional (2D) PL spectra of octadecyl-passivated SiQDs both before and after wet oxidation treatment. The analysis indicates that the wet oxidation-treated SiQDs exhibit PL in the NUVV region (NUVV-QDs), whereas the control sample displays PL in the NIR region (NIR-QDs). Notably, this method facilitates a complete transition from NIR to NUVV emission without the formation of an intermediate state that contains both emission bands, as illustrated in Fig. S2. As depicted in Fig. 2(d), the narrow-band spectrum of the excitation light (the region outlined by the white dashed line) is inevitably captured during detection due to the close proximity of the NUVV emission and excitation wavelengths. Since our focus is solely on the spectra of the samples, the excitation light spectra have been subtracted from the subsequent extraction of the PL and photoluminescence excitation (PLE) spectra. Fig. 2(b) and (e) display the PL, PLE, and UV-Vis

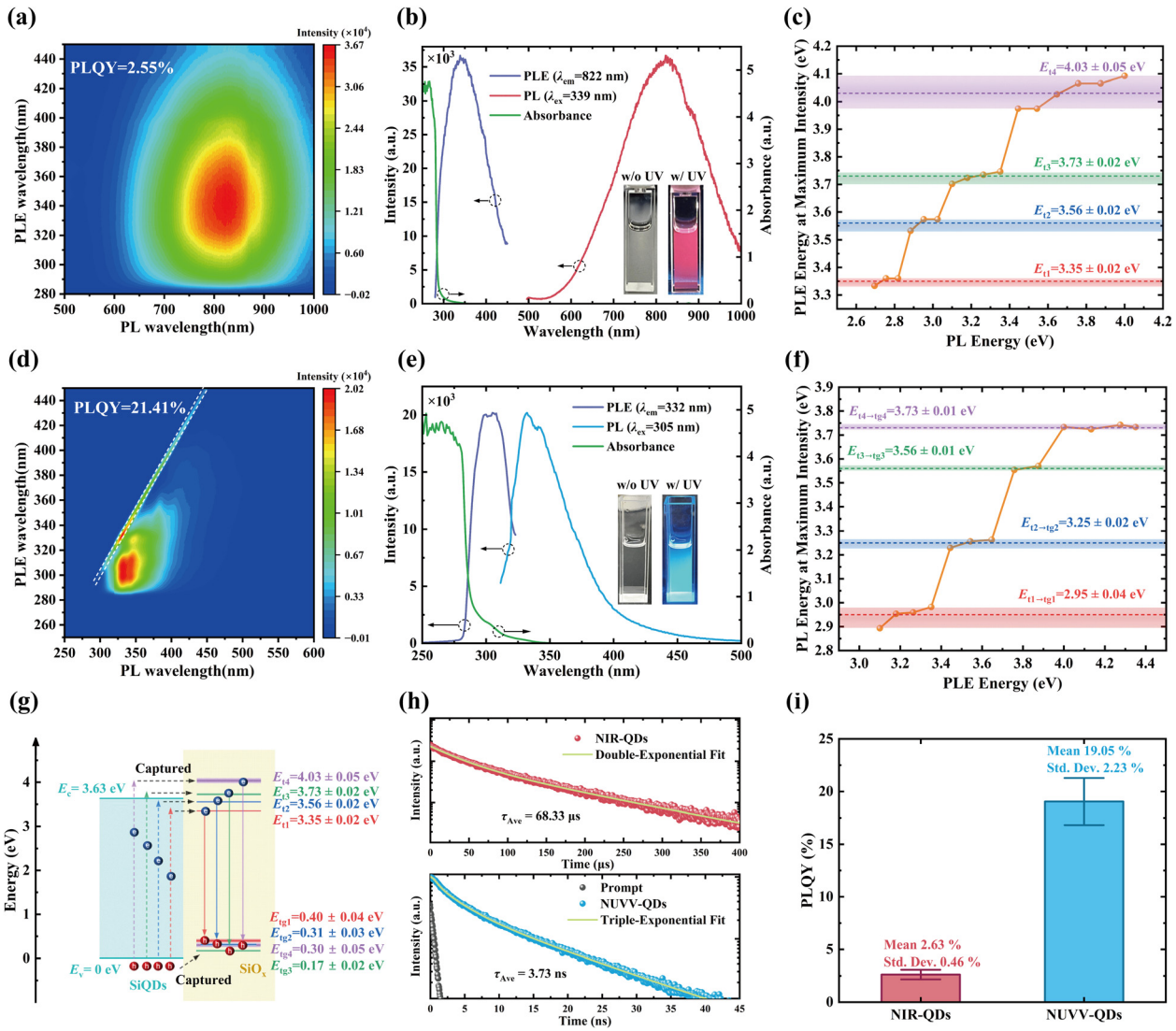

Fig. 2 (a) Two-dimensional PL spectra of the NIR-QDs. (b) PLE, PL and absorption spectra of the NIR-QDs. (c) Evolution of PLE peak energy with PL energy for the NUVV-QDs (the shaded regions indicate the range for each stage, while the dashed lines represent the mean values). (d) Two-dimensional PL spectra of the NUVV-QDs (the dashed line denotes the collected excitation light spectrum). (e) PLE, PL and absorption spectra of the NUVV-QDs. (f) Evolution of PL peak energy with PLE energy for the NUVV-QDs (the shaded regions indicate the range for each stage, while the dashed lines represent the mean values). (g) The potential mechanism for the excitation and emission of the NUVV-QDs. (h) PL decay profiles of NIR-QDs and NUVV-QDs. (i) Statistical results of the PLQY of the NIR-QDs and NUVV-QDs.

absorption spectra of these two types of QDs. The PL wavelengths exhibiting the highest emission intensity for NIR-QDs and NUVV-QDs are 822 nm (1.51 eV) and 332 nm (3.73 eV), corresponding to excitation wavelengths of 339 nm (3.66 eV) and 305 nm (4.07 eV), respectively. The insets present the photographs of these two quantum dots illuminated by visible light and subjected to 365 nm UV irradiation. NIR-QDs and NUVV-QDs exhibit light red and sky-blue coloration under UV irradiation, corresponding to the visible components of their respective emission spectra. Fig. S3 and S4 illustrate the evolution of the PLE spectra as a function of the PL wavelength and the evolution of the PL spectra as a function of the PLE wavelength for both QDs. The maximum of the PLE spectra for the NIR-QDs is located at 342 nm and exhibits a negligible variation with changes in the PL wavelength, indicating that the direct bandgap of the NIR-QDs is 3.63 eV. Moreover, the maximum of the PL spectra for the NIR-QDs is located at 822 nm and shows a negligible variation with changes in the PLE wavelength, suggesting that the emission of the NIR-QDs arises from the Γ–X transition with an indirect bandgap of 1.51 eV.[67] The maximum of the PLE spectra of the NUVV-QDs experiences a significant redshift with an increasing PL wavelength, accompanied by the presence of ten distinguishable shoulders. Similarly, the maximum of the PL spectra of the NUVV-QDs exhibits a notable redshift with an increasing PLE wavelength, accompanied by nine distinguishable shoulders. This excitation dependence of the PL suggests that the observed emission originates from trap states introduced by oxides or ligands on the surfaces of SiQDs, rather than from intrinsic emission (indirect Γ–X transition) of the silicon core.[65,67] Furthermore, the emission dependence of the PLE further implies that these trap states are also involved in the excitation process. Notably, the emissions of the multiple peaks may also arise from the vibronic structure associated with the surface groups. However, it is important to note that the wavenumber spacing between the nine emission subpeaks ranges from 419 to 1587 cm^{-1}, with these spacings being unequal. This uneven spacing indicates that the multiple peak emissions do not stem from the vibronic structure.

To identify the energy levels of the trap states, we analyzed the dependence of the PLE peak wavelength of the NUVV-QDs on the PL wavelength, as illustrated in Fig. 2(c). Four distinct steps in the PLE peak wavelength can be identified, which are attributed to four trap states (E_t). By calculating the average energy of these components, the relative energy levels of the four trap states were obtained, with the energy level of the valence band maximum (VBM) of the NUVV-SiQDs set to 0 eV: E_{t1} = 3.35 ± 0.02 eV, E_{t2} = 3.56 ± 0.02 eV, E_{t3} = 3.73 ± 0.02 eV, and E_{t4} = 4.03 ± 0.05 eV. The shaded regions in Fig. 2(c) indicate the range for each stage, while the dashed lines represent the mean values. To identify the emission characteristics of the trap states, the dependence of the PL peak wavelength of the NUVV-QDs on the PLE wavelength is illustrated in Fig. 2(f). Notably, the PL peak wavelength also exhibits four distinct steps, corresponding to the four trap states. The emission energies of these trap states were determined by calculating the average energies of the four components, which are as follows: 2.95 ± 0.04 eV, 3.25 ± 0.02 eV, 3.56 ± 0.01 eV, and 3.73 ± 0.01 eV. The shaded regions in Fig. 2(f) indicate the ranges corresponding to each stage, while the dashed lines denote the mean values. These four emission energies demonstrate significant redshifts relative to the energy levels of the trap states, indicating that electrons in the trap states transition to trap ground states (E_{tg}) with higher energies than the SiQD VBM for radiative recombination, rather than transitioning directly to the SiQD VBM. Therefore, these four energies can be denoted as $E_{ti\rightarrow tgi}$ (i = 1, 2, 3, 4). By calculating the average value of E_{ti}–$E_{ti\rightarrow tgi}$, we can derive: E_{tg1} = 0.40 ± 0.04 eV, E_{tg2} = 0.31 ± 0.03 eV, E_{tg3} = 0.17 ± 0.02 eV, and E_{tg4} = 0.30 ± 0.05 eV. Additionally, it is noted that the PL spectra of both QDs nearly disappear when the excitation energy reaches 4.43 eV (280 nm) (see Fig. S3 and S4). This phenomenon is attributed to the substantial absorption of excitation light at 280 nm by toluene, the solvent used. As illustrated in Fig. S5, the absorbance of pure toluene at excitation wavelengths of 280 nm, 285 nm, and 290 nm is measured at 3.55, 0.69, and 0.21, respectively. The absorbance of the SiQD toluene solution at the same excitation wavelengths is measured at 4.19, 1.71, and 0.80, respectively. Utilizing the Beer–Lambert law (with a 1-cm transmission path),[78] the transmittance of pure toluene is calculated to be 0.03%, 20.42%, and 61.66%, while that of the SiQD toluene solutions is 0.006%, 1.95%, and 15.85%, respectively. The disparity in transmittance between pure toluene and SiQD solutions provides a rough estimation of the light absorption ability of the SiQDs. Notably, at an excitation wavelength of 280 nm, the transmittance difference is 0.024%, indicating that SiQDs exhibit negligible absorption of the excitation light. Conversely, at excitation wavelengths of 285 nm and 290 nm, the transmittance difference exceeds 18.47%, indicating substantial absorption of excitation light by SiQDs, which aligns with the observation of discernible PL spectra. Based on the preceding discussion, we propose a potential mechanism for the excitation and emission of NUVV-QDs (Fig. 2(g)), which is similar to the mechanism identified for violet-blue emission in SiQDs by Yang *et al.*[76]

As illustrated in Fig. 2(h), the PL decay profiles of both NIR-QDs and NUVV-QDs were fitted using double and triple exponential functions. Table 1 presents the lifetimes derived from the fitting, along with the normalized amplitudes. The average PL lifetime of the NIR-QDs is 68.33 μs, consistent with the average lifetime of SiQDs exhibiting the S-band emission (microsecond range) reported in the literature.[65,72] This finding further substantiates that the emission from the NIR-QDs originates from the indirect transition of Γ–X. In contrast,

Table 1 PL lifetimes and normalized amplitudes of NIR-QDs and NUVV-QDs

Sample	B_1	τ_1	B_2	τ_2	B_3	τ_3	τ_{ave}
NIR-QDs	0.60	35.67 μs	0.40	116.59 μs	—	—	68.33 μs
NUVV-QDs	0.31	3.36 ns	0.21	11.21 ns	0.47	0.62 ns	3.73 ns

the average PL lifetime of the NUVV-QDs is 3.73 ns, aligning with the average lifetime of SiQDs with the F-band emission (nanosecond range) found in the literature.[65,72] This result supports the assertion that the emission from the NUVV-QDs arises from surface states or defect states rather than from band transitions. Additionally, the PL spectrum used for measuring the PL lifetime (λ_{ex} = 317 nm) was decomposed using Gaussian functions based on the peak positions of the nine shoulders in the PL spectra, resulting in Fig. S6. The cumulative fit curve demonstrates a strong alignment with the PL data. Since the PL wavelength captured during the PL decay measurement is 350 nm (dashed line in Fig. S5), it can be inferred that the three components of the PL decay correspond to the subpeaks at 346 nm (component B_1), 362 nm (component B_2), and 344 nm (component B_3), respectively. All three subpeaks are attributed to the emissions from the $E_{t3\rightarrow tg3}$ processes. Consequently, the electron, upon being trapped by the E_{t3} trap state, relaxes to a lower-energy sub-trap state before undergoing radiative transition. This relaxation to the lower-energy sub-trap state requires additional time, which accounts for the ordering of the PL lifetimes of the three subpeaks.

Fig. 2(i) presents the statistical results of the PLQY for NIR-QDs and NUVV-QDs, with the error bars representing one standard deviation. The average PLQY of the NUVV-QDs is measured at 19.05%, which is a 6.24-fold increase over that of the NIR-QDs. This enhancement may be attributed to the wet oxidation treatment, which effectively passivates the dangling bond defects on the surface of the SiQDs. Notably, multiple samples of NUVV-QDs were prepared to assess the reproducibility of the synthesis method, as illustrated in Fig. S7. The PL spectra of these samples exhibited consistent shapes and comparable PLQYs, confirming the high reproducibility of the wet oxidation treatment.

3.2. Exclusion of NUVV emission as intrinsic or by-product emission

According to the literature, the NUVV emission is proposed to originate from three potential sources: (1) intrinsic emission from the Si core (<1.53 nm),[67,79] (2) surface-related radiative recombination,[24,40,71,72] and (3) the by-product carbon quantum dots (CQDs) formed during the reaction process.[68,80] While the PLE and PL spectra of NUVV-QDs indicate that the NUVV emission arises from recombination involving trap states introduced by oxides or ligands on the surface of the quantum dots, it remains essential to exclude scenarios (1) and (3).

Fig. 3(a) and (d) present TEM images of NIR-QDs and NUVV-QDs. Particle size analysis reveals that the average diameters (d_{TEM}) of NIR-QDs and NUVV-QDs are 4.78 ± 0.16 nm and 4.95 ± 0.11 nm, respectively, as illustrated in Fig. 3(c) and (f). If the NUVV emission originates from the silicon core, the diameter of the SiQDs would need to be below 1.53 nm, as determined using the EMA method.[66] Moreover, the size difference between the two quantum dots is less than 0.2 nm, which is insufficient to account for the transition from NIR to

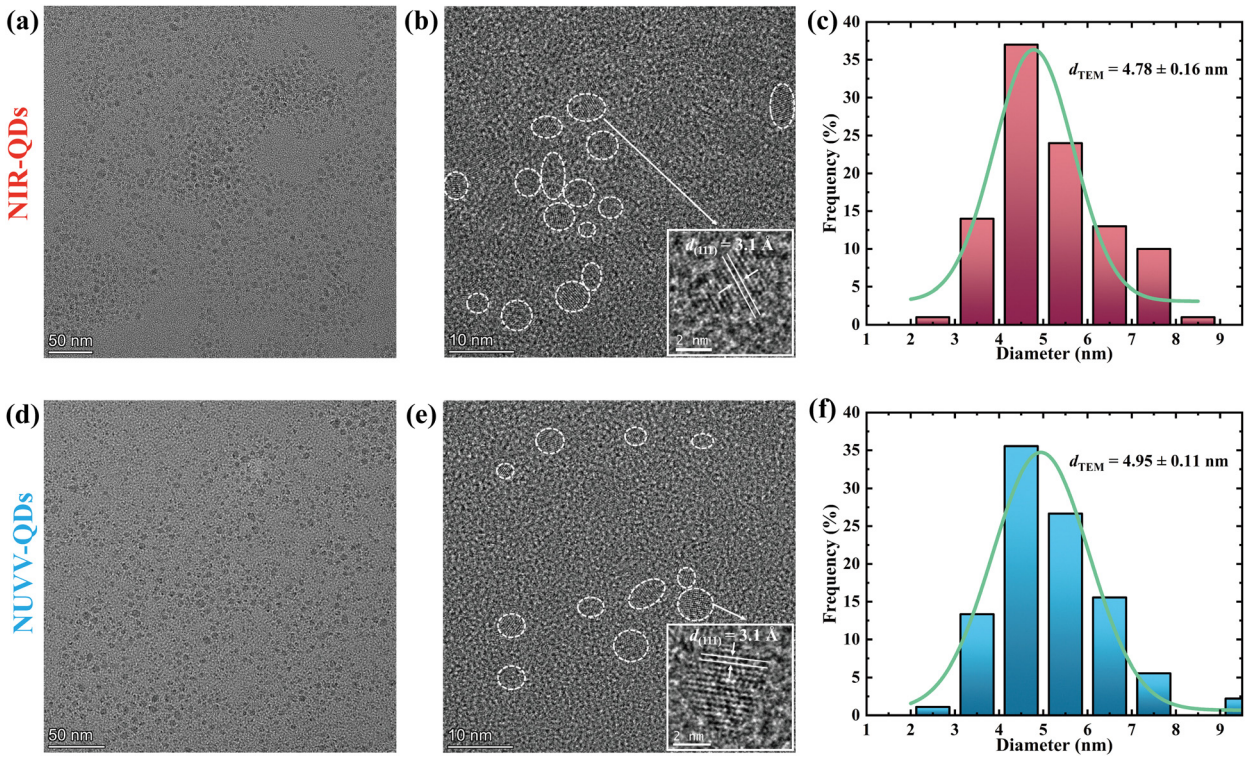

Fig. 3 (a) TEM images of the NIR-QDs. (b) HR-TEM images of the NIR-QDs (the inset is the zoomed-in view of a QD). (c) Particle size distribution statistics of the NIR-QDs. (d) TEM images of the NUVV-QDs. (e) HR-TEM images of the NUVV-QDs (the inset is the zoomed-in view of a QD). (f) Particle size distribution statistics of the NUVV-QDs.

NUVV emission. Consequently, the possibility that the NUVV emission represents intrinsic emission can be ruled out. Fig. 3(b) and (e) present HR-TEM images of NIR-QDs and NUVV-QDs. Both quantum dots exhibit clear lattice fringes and possess a *d*-spacing of 0.31 nm, corresponding to the (111) plane of the diamond cubic lattice of silicon.[81,82] This finding substantiates that both NIR-QDs and NUVV-QDs are SiQDs, thereby ruling out the possibility that NUVV-QDs are CQDs. It is noteworthy that the diameter of the NUVV-QDs increases by approximately 0.2 nm relative to that of the NIR-QDs, which may result from the coverage or ligands on the surface of the SiQDs.

Given that the primary difference between NIR-QDs and NUVV-QDs lies in the presence or absence of wet oxidation, the surface coverage responsible for NUVV PL is most likely SiO_x. Additionally, the ligands potentially contributing to the NUVV PL are hypothesized to include siloxane groups (Si–O–Si), hydroxyl groups (Si–OH), or ethoxy groups (Si–OC_2H_5). Therefore, further characterization is necessary to ascertain which of these factors is responsible for the NUVV emission. Overall, the TEM results suggest that the NUVV emission is surface-related.

3.3. Crystalline analysis of SiQDs

The wet oxidation process was performed following HF etching and prior to hydrosilylation. This sequence enables an accurate assessment of the presence or absence of SiO_2 on the SiQD surface, as well as the crystalline structure of SiQDs, through the XRD and Raman patterns of the hydrogen-passivated SiQDs. Fig. 4 presents the XRD patterns of two types of hydrogen-passivated SiQDs (after drying under argon or ambient air). The patterns exhibit diffraction peaks at 28°, 47°, and 56°, which correspond to the (111), (220), and (311) planes of the diamond cubic lattice of silicon,[45] respectively. The diffraction peaks for SiO_2 were not observed at approximately 22° in the patterns of both NIR-QDs and NUVV-QDs. It is important to note that the random bond (RB) model is commonly employed to elucidate the structure of SiO_x.[83] The RB model posits that the SiO_x structure consists of a random distribution of Si–Si and Si–O bonds, which permeate the entire structural network.[83] In essence, the RB model suggests that SiO_x is amorphous; thus, the absence of SiO_2 diffraction peaks aligns with the presence of SiO_x consistent with the RB model. This indicates that SiO_x may be present, which is consistent with the results observed in the previously mentioned PL spectra. Additionally, the crystal sizes (d_{XRD}) of the two types of QDs were calculated to be 4.77 ± 0.48 nm and 4.93 ± 0.65 nm, respectively, using the Scherrer equation.[1] These results show excellent agreement with the d_{TEM}.

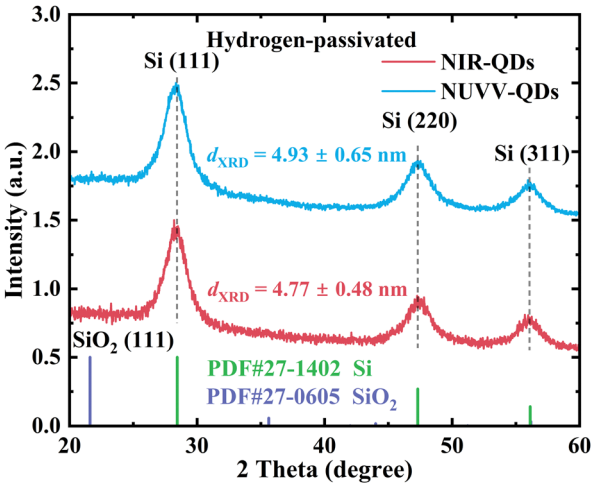

Fig. 4 XRD patterns of the hydrogen-passivated SiQDs after drying under argon and ambient air.

Fig. 5(a) and (b) show the Raman spectra of two types of hydrogen-passivated SiQDs. The literature indicates that the fitted curves of the Raman spectra for silicon can be decomposed into amorphous (503–504 cm^{-1}) and crystalline (512–516 cm^{-1}) components using two Gaussian functions.[77] The Raman peaks for crystalline silicon in the NIR-QDs and NUVV-QDs are located at 515.63 cm^{-1} and 512.64 cm^{-1}, respectively, exhibiting significant redshifts relative to the Raman peak of bulk silicon at 521 cm^{-1}.[84] The peak wavenumbers of the silicon nanocrystals can be calculated based on the phonon confinement model:[84]

$$\omega(d) = \omega_0 - 47.41 \cdot \left(\frac{a}{d}\right)^{1.44} \quad (1)$$

where ω_0 represents the peak wavenumber of bulk silicon (521 cm^{-1}), d is the crystal size of the SiQDs (*i.e.*, d_{XRD}), and a is the lattice constant of crystalline silicon (0.543 nm). Under consideration of phonon confinement only, the peak wavenumbers for crystalline silicon in NIR-QDs and NUVV-QDs are calculated to be 518.92 cm^{-1} and 519.02 cm^{-1}, respectively, which are higher than the experimental values. This discrepancy arises because the phonon confinement model assumes that the surfaces of the silicon nanocrystals are free of ligands and coverage.[84] In reality, the ligands and coverage exert tensile stresses on the SiQDs, which causes a redshift in the Raman peak. According to the literature, the tensile stress (σ) can be calculated as follows:[84]

$$\sigma = \frac{\Delta\omega}{-\kappa} \quad (2)$$

where $\Delta\omega$ represents the shift relative to the initial peak wavenumber (*i.e.*, phonon-induced peak wavenumber) at ambient pressure, and κ denotes the wavenumber stress factor (κ = −4.27). Fig. 5(c) presents the statistical results of the tensile stress on the two types of SiQDs. This indicates that there is a higher density of ligands or coverage (SiO_x) on the surface of the NUVV-QDs, thereby exerting greater tensile stress. Additionally, the crystalline fraction (f_c) of SiQDs, which reflects the degree of crystallinity of the SiQDs, can be derived from the integrated intensities of the crystalline and amorphous silicon components:[85]

$$f_c = \frac{1}{1 + \gamma \cdot (I_a/I_c)} \quad (3)$$

$$\gamma = 0.1 + 0.9e^{-L} \quad (4)$$

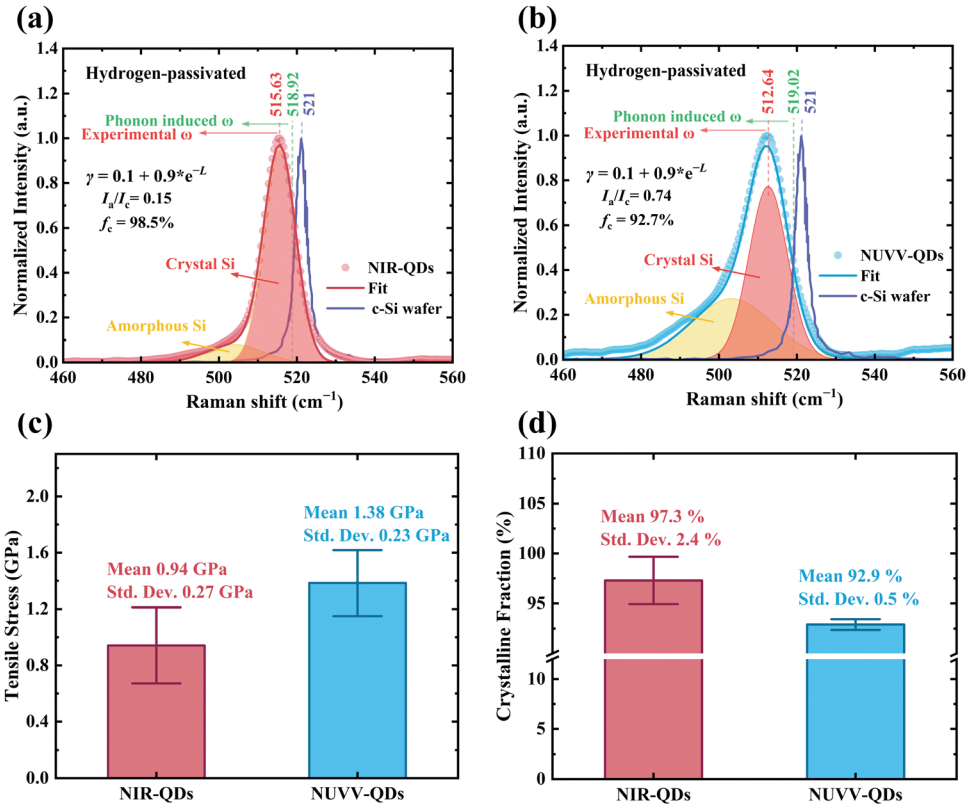

Fig. 5 (a) and (b) Raman spectra of the hydrogen-passivated SiQDs after drying under argon and ambient air. (c) Tensile stress on the surface of the hydrogen-passivated SiQDs after drying under argon and ambient air. (d) Crystalline fractions of the hydrogen-passivated SiQDs after drying under argon and ambient air.

where I_a is the integrated intensity of the amorphous silicon component, I_c is the integrated intensity of the crystalline silicon component, γ is the relative Raman cross-section, and L is the crystal size of silicon (*i.e.*, d_{XRD}). Fig. 5(d) displays the statistical results of the crystalline fraction of the two types of SiQDs. It is observed that the f_c of the NUVV-QDs is significantly lower than that of the NIR-QDs, which is attributed to the amorphization caused by greater tensile stress.[72] The results for f_c provide further evidence of the greater tensile stress on NUVV-QDs, suggesting a higher density of ligands or coverage (SiO_x) on the surface of the NUVV-QDs.

3.4. Surface and defect analysis of SiQDs

The ATR-FTIR spectra of NIR-QDs and NUVV-QDs are shown in Fig. 6. The observed absorption bands at 3360 cm^{-1}, 2954 cm^{-1}, 2920 (2851) cm^{-1}, 1745–1739 cm^{-1}, 1461–1460 cm^{-1}, 1377 cm^{-1}, and 720 cm^{-1} correspond to O–H stretching,[86] CH_3 stretching,[47] CH_2 stretching,[47] C═O stretching,[26,30] CH_2 bending,[47] CH_3 bending,[47] and CH bending modes,[87] respectively. In addition, absorption bands at 1263–1249 cm^{-1}, 1190–1189 (1082–1081) cm^{-1}, 1158–1157 cm^{-1}, 968–967 (849–848) cm^{-1}, and 908 cm^{-1} are assigned to Si–C stretching,[75] Si–O–Si stretching,[74] C–O stretching,[88] Si–H bending,[37,75] and Si–OH stretching modes,[45] respectively. The locations and normalized intensities of the various groups are summarized in Table 2 for comparative analysis.

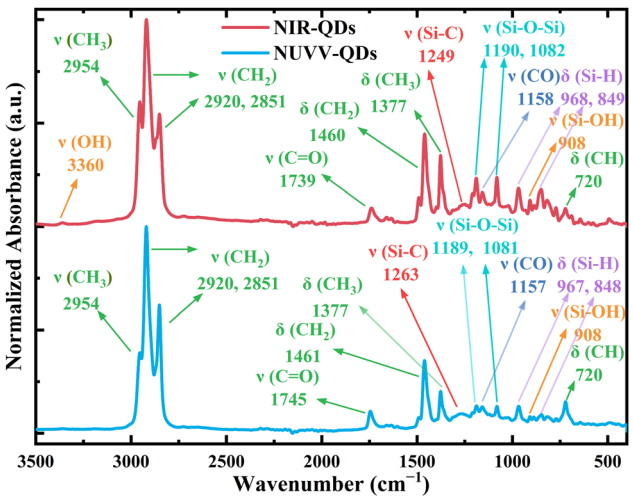

Fig. 6 ATR-FTIR spectra of NIR-QDs and NUVV-QDs.

The intensities of the Si–C, Si–O–Si, Si–H, Si–OH, and C–O bands for the NIR-QDs are significantly higher than those for the NUVV-QDs, suggesting that the densities of Si–C, Si–O–Si, Si–H, Si–OH, and Si–OC_2H_5 groups on the surface of the NIR-QDs are substantially greater than those of the NUVV-QDs. However, this finding indicates that neither Si–O–Si, Si–OH, nor Si–OC_2H_5 groups are directly responsible for NUVV emission.

Table 2 Assignments of the FTIR spectra of NIR-QDs and NUVV-QDs

Wavenumber (cm^{-1})	Assignment	Normalized absorbance		Ref.
		NIR-QDs	NUVV-QDs	
3360	O–H stretching	0.018	—	86
2954	CH_3 stretching	0.603	0.390	47
2920, 2851	CH_2 stretching	1, 0.544	1, 0.620	47
1745–1739	C═O stretching	0.090	0.107	26 and 30
1461–1460	CH_2 bending	0.448	0.352	47
1377	CH_3 bending	0.343	0.203	47
1263–1249	Si–C stretching	0.108	0.094	75
1190–1189, 1082–1081	Si–O–Si stretching	0.233, 0.237	0.131, 0.130	74
1158–1157	C–O stretching	0.164	0.128	88
968–967, 849–848	Si–H bending	0.184, 0.179	0.131, 0.091	37 and 75
908	Si–OH stretching	0.128	0.081	45
720	CH bending	0.087	0.152	87

Additionally, NUVV-QDs exhibit weaker group vibrational intensities in the range of 908 to 1461 cm^{-1} compared to NIR-QDs, thereby further excluding the possibility that the NUVV emission arises from the vibronic structure. According to the literature,[40] when the dangling bonds of SiQDs are exposed to ethanol, they undergo three key processes that result in oxidation: surface alkoxylation, hydrolysis, and condensation. These processes convert the dangling bonds first to Si–OC_2H_5, then to Si–OH, and finally to Si–O–Si groups. Furthermore, since the Si–O bond exhibits higher stability than the Si–H bond,[40,89] it can be inferred that the Si–H bonds on the SiQDs also react with ethanol to form Si–OC_2H_5. This reaction is followed by the formation of Si–OH groups and subsequently Si–O–Si groups.

DeBenedetti *et al.* demonstrated that the rate of oxidation reactions involving ethanol increases under conditions of higher concentrations of O_2 or elevated temperatures.[40] In contrast, in the absence of alcohols, the dangling bonds and Si–H bonds in SiQDs exposed to air can react with oxygen to form Si–O–Si and Si–OH groups, with Si–OH later converting into Si–O–Si.[90,91] Therefore, it could be expected that the surface of the NUVV-QDs would exhibit a higher density of oxygen-related groups due to their exposure to air. However, in this study, the densities of the three groups (*i.e.*, Si–OC_2H_5, Si–OH, and Si–O–Si) are higher in NIR-QDs than those in NUVV-QDs, contrary to expectations. From the above observations, we suggest the following mechanism for the wet oxidation process: (1) Dangling bonds and Si–H bonds on the surface of SiQDs react with ethanol to form Si–OC_2H_5 groups. (2) Subsequently, the presence of H_2O in air leads to an intense hydrolysis of Si–OC_2H_5 groups, resulting in an increased number of Si–OH groups. At the same time, O_2 reacts directly with Si–H bonds, forming additional Si–OH groups. (3) Ultimately, a significant number of Si–OH groups condense into the SiO_x networks. This process generates numerous oxygen-related defects due to incomplete cross-linking or residual Si–OH groups, rather than forming uniform Si–O–Si groups. Under argon drying conditions, the only source of H_2O that can react with Si–OC_2H_5 is the residual moisture from the etching solution. Additionally, the absence of O_2 inhibits the conversion of Si–H to Si–OH. As a result, the density of converted Si–OH groups is significantly lower than that under air drying conditions. Therefore, the accelerated group conversion processes under air drying conditions (≡Si·/Si–H ↔ Si–OC_2H_5 → Si–OH → SiO_x and ≡Si· ↔ Si–H → Si–OH → SiO_x) account for the lower densities of dangling bonds, Si–H bonds, and Si–OC_2H_5, Si–OH, and Si–O–Si groups in NUVV-QDs. Additionally, during the hydrosilylation stage, the sites in NUVV-QDs that can be converted into Si–C groups (Si–H bonds and dangling bonds) are fewer than those in NIR-QDs, thereby resulting in a reduced number of potential Si–C groups. Consequently, the NUVV-QDs after hydrosilylation have a lower density of octadecyl coverage. It is noteworthy that the carbonyl group (C═O), which is absent in both ethanol and octadecene, was detected in both types of QDs. The absorbance of C═O and CH groups is higher in NUVV-QDs than that in NIR-QDs, suggesting that the C═O group originates from the oxidation of the CH_3 group, which occurs more intensively under air conditions. This suggests that NUVV-QDs have undergone more intensive oxidation, supporting the possibility of SiO_x formation, as previously described. Therefore, it can be inferred that SiO_x with oxygen-related defects on the surface of SiQDs is responsible for the NUVV emission.

Conventionally, the types of oxygen-related defects in SiO_x include peroxy linkage (POL, *i.e.*, ≡Si–O–O–Si≡), oxygen-deficient center (ODC(I) or ODC(II), *i.e.*, ≡Si–Si≡ or ═Si:), E′ centers (E′, *i.e.*, ≡Si·), non-bridging oxygen hole center (NBOHC, *i.e.*, ≡Si–O(h^+)), and self-trapped exciton (STE, *i.e.*, ≡Si(e^-)···(h^+)O–Si≡).[92,93] To assess the types of defects, EPR measurements were performed on NIR-QDs and NUVV-QDs, as illustrated in Fig. 7(a). Notably, the E′ features (g_1 = 2.0018, g_2 = 2.0006, g_3 = 2.0003) are absent in the EPR spectra of the NUVV-QDs,[94] indicating the absence of this type of defect. Additionally, the PL emission energies for POL, ODC(I), ODC(II), NBOHC, and STE are 3.49 eV,[95] 2.7 eV,[93,96] 4.4 eV,[93] 1.9 eV,[93] and 2.3 eV,[92] respectively. Comparatively, the PL emission energies of the NUVV-QDs range from 2.95 eV to 3.73 eV, suggesting that the defect types present in NUVV-QDs include POL and ODC(I). Therefore, trap states E_{t1} and E_{t2} (trap ground states E_{tg1} and E_{tg2}) are associated with ODCs(I), while trap states E_{t3} and E_{t4} (trap ground states E_{tg3} and E_{tg4}) are linked to POLs. Based on the PLE and PL spectra of NUVV-QDs (Fig. S3 and S4), the density of POLs is found to be higher than

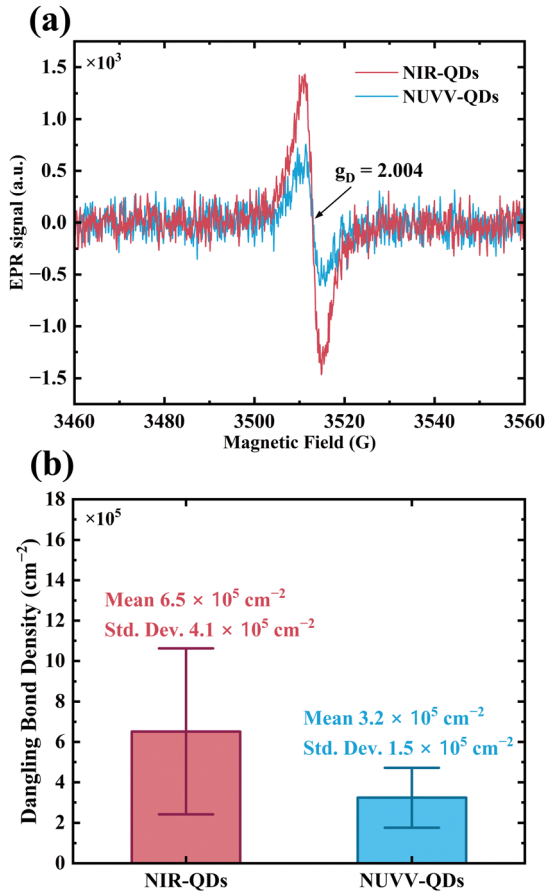

Fig. 7 (a) EPR spectra of the NIR-QDs and NUVV-QDs. (b) Density of dangling bonds on the surface of the NIR-QDs and NUVV-QDs.

that of ODCs(I). The large tensile stress observed in NUVV-QDs, derived from Raman results, is consistent with the dominance of POLs. We suggest that oxygen from the air supplies additional oxygen atoms for the Si–O–Si groups, resulting in a high density of POLs. Furthermore, the EPR curves of two types of QDs exhibit peak-to-valley transition signals near a magnetic field of 3513 G, corresponding to a g-factor value of 2.004. This pattern is indicative of dangling bonds (D centers) on the surface of SiQDs.[59] Notably, the EPR signals of the NUVV-QDs are significantly weaker than those of the NIR-QDs, suggesting a lower density of dangling bonds on the surface of NUVV-QDs. By double integrating the EPR spectra of the samples (*i.e.*, integrating twice to calculate the total spin density) and using DPPH at a concentration of 10^{-3} mol L^{-1} as a reference, the density of dangling bonds (A_{db}) on the surface of SiQDs can be quantitatively calculated,[59,97,98] as shown in Fig. 7(b). It is evident that the average A_{db} of NUVV-QDs is only half that of the NIR-QDs, indicating that the wet oxidation treatment effectively reduces dangling bonds on the surface of SiQDs. This is attributed to the presence of O_2 and H_2O, which facilitates the conversion of more Si–OC_2H_5 groups and Si–H bonds into Si–OH groups ($\equiv$Si·/Si–H ↔ Si–OC_2H_5 → Si–OH and $\equiv$Si· ↔ Si–H → Si–OH). These groups subsequently condense to form SiO_x networks that contain POLs and ODCs(I). This transformation implies a reduction in nonradiative recombination and an enhancement of trap-induced emission, which may explain why NUVV-QDs exhibit a PLQY 6.24 times (Fig. 2(i)) higher than that of NIR-QDs.

3.5. Formation processes and emission mechanisms of NUVV-emitting SiQDs

Depending on the preceding discussions, we delineate the formation processes of NIR-QDs and NUVV-QDs, as depicted in Fig. 8. Upon etching the pyrolysis products with HF, SiQDs are liberated from the SiO_2 matrix. The literature shows that dangling bonds, Si–H bonds, and Si–OH groups are present on the surfaces of freshly etched SiQDs.[74,75] Subsequently, the drying atmosphere significantly influences the final surface composition, resulting in the formation of NIR-QDs and NUVV-QDs through drying under argon and ambient air, respectively.

The oxidation process during argon drying follows these steps: (1) The dangling bonds and Si–H bonds on the surface of SiQDs react with C_2H_5OH to form Si–OC_2H_5 groups. (2) The Si–OC_2H_5 groups hydrolyze with H_2O from the residual etching solution, resulting in the formation of Si–OH. (3) Adjacent Si–OH groups condense to generate Si–O–Si groups. Following hydrosilylation, some Si–H bonds and dangling bonds are converted into octadecyl groups. Since the dissociation energies of Si–O and Si–OH bonds (540 kJ mol^{-1}) significantly exceed those of Si–H (335 kJ mol^{-1}) and Si–C (370 kJ mol^{-1}),[89] the temperature employed for hydrosilylation is unlikely to cleave Si–O and Si–OH bonds. The oxidation process in ambient air (15–25 °C, 30–55% RH) unfolds as follows: (1) The reaction mechanism is the same as that in step (1) during argon drying. (2) Hydrolysis of the Si–OC_2H_5 groups with H_2O from the air forms Si–OH groups. Additionally, Si–H groups are oxidized by O_2, thereby producing Si–OH groups. The rate of Si–OH generation under these conditions is markedly faster than that observed in argon drying. (3) The rapidly generated Si–OH groups condense in large quantities, forming SiO_x networks characterized by two oxygen-related defects: POLs and ODCs(I), rather than simple Si–O–Si groups. Additionally, a small number of adjacent Si–OH groups also condense to form Si–O–Si groups. After hydrosilylation, the number of Si–H bonds and dangling bonds in NUVV-QDs that are effectively converted into octadecyl groups is smaller than that in NIR-QDs, resulting in a reduced octadecyl coverage compared to argon drying conditions.

Overall, wet oxidation primarily relies on ethanol, H_2O, and O_2. In the absence of ethanol, only trace amounts of Si–OH is present on the surface of SiQDs following HF etching. By contrast, ethanol significantly converts numerous dangling bonds and Si–H bonds into Si–OC_2H_5 groups, which determines the potential number of Si–OH groups generated through hydrolysis. H_2O in the air effectively converts Si–OC_2H_5 into Si–OH groups, facilitating extensive condensation and the formation of SiO_x networks containing oxygen-related defects. Additionally, O_2 in the air reacts with Si–H to form more Si–OH groups, while it also supplies sufficient oxygen atoms for the generation of POLs. Therefore, the alkoxylation induced by

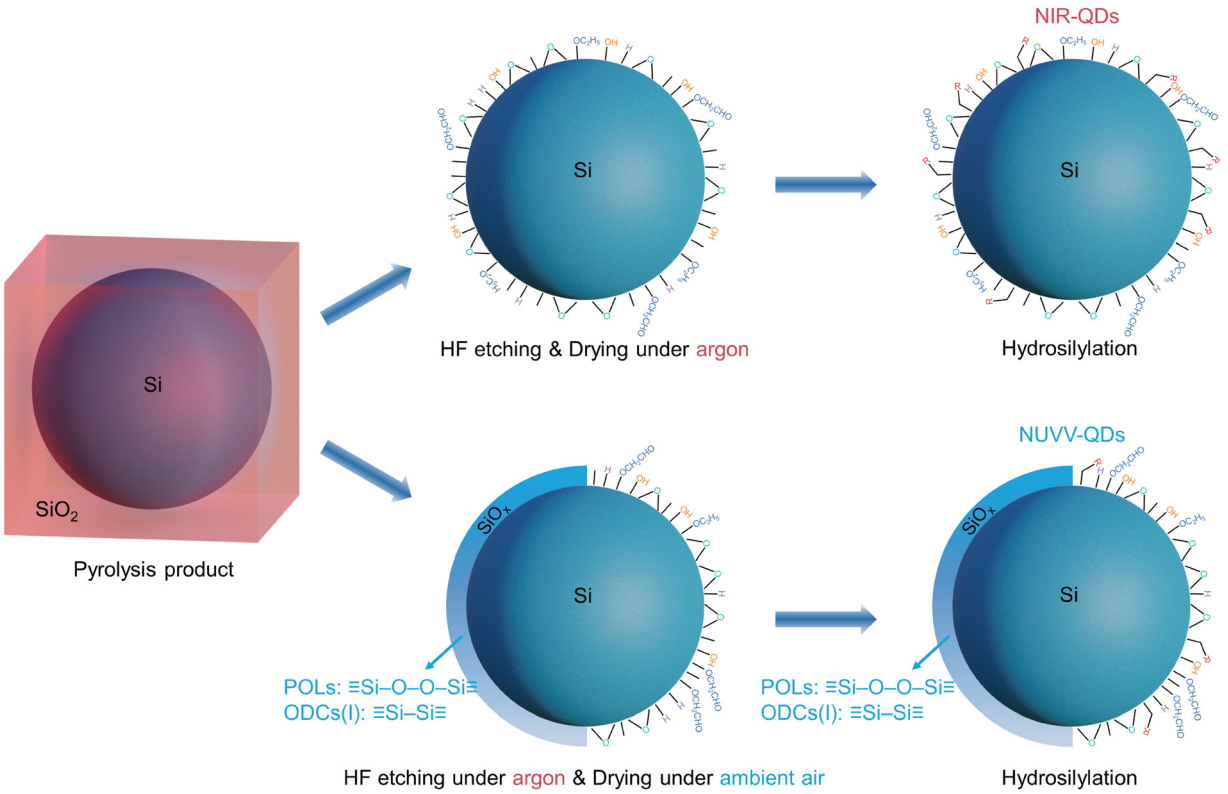

Fig. 8 A schematic diagram of the formation of NIR-QDs and NUVV-QDs.

ethanol serves as the foundation for wet oxidation, while H_2O and O_2 act as essential components for the complete progression of the wet oxidation reaction.

Before analyzing the emission mechanisms of NUVV-QDs, it is essential to address several key concepts. The NIR emission originates from the indirect Γ–X transition, which is attributed to the intrinsic radiative recombination within the Si core. We suggest that the single initial NIR radiative state resides at the CBM, with the bandgap energy determined by the QD size. The observation of an unshifted PL peak in NIR-QDs (Fig. S3) supports this hypothesis. Dangling bonds introduce nonradiative defect states within both the direct Γ–Γ and the indirect Γ–X bandgaps, enabling the trapped electrons to release energy by nonradiative recombination. Notably, the wet oxidation treatment resulted in the formation of SiO_x with two types of oxygen-related defects on the surface of SiQDs, leading to the introduction of four trap states and four trap ground states associated with NUVV emission. These trap states are termed E_{t1} and E_{t2} for ODCs(I) and E_{t3} and E_{t4} for POLs. Trap ground states are termed E_{tg1} and E_{tg2} for ODCs(I) and E_{tg3} and E_{tg4} for POLs. As illustrated in Fig. 9, the emission process of NUVV-QDs comprises four main stages: (1) Electrons within the SiQDs absorb UV light, undergoing a direct Γ–Γ transition. (2) A subset of electrons in the CBM of the SiQDs relaxes to nonradiative trap states introduced by dangling bonds, releasing energy as phonons. Subsequently, they detach from these trap states and further relax to the VBM, again releasing energy in the form of phonons. (3) Most excited or quasi-excited state

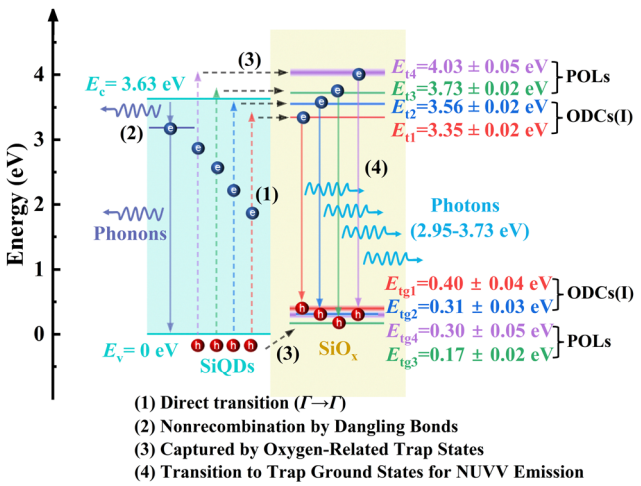

Fig. 9 A schematic diagram of the emission mechanisms of NUVV-QDs.

electrons in proximity to the CBM of the SiQDs are captured by radiative trap states induced by oxygen-related defects in SiO_x. Additionally, holes at the VBM are captured by the trap ground states introduced by oxygen-related defects. (4) The trapped electrons are released from radiative trap states and transition to the trap ground states, where they recombine with holes, emitting 2.95–3.73 eV of energy in the form of photons. For ODC(I) defects, the emitted energies are 2.95 ± 0.04 eV ($E_{t1\rightarrow tg1}$) and 3.25 ± 0.02 eV ($E_{t2\rightarrow tg2}$), while for POL defects, the emitted energies are 3.56 ± 0.01 eV($E_{t3\rightarrow tg3}$) and 3.73 ± 0.01 eV

($E_{t4\rightarrow tg4}$). Furthermore, the emission induced by POLs is the primary contributor, followed by that induced by ODCs(I). Based on the formation process and the emission mechanism of NUVV-QDs, the significantly enhanced PLQY compared to the NIR counterparts can be attributed to two main factors: (1) The presence of H_2O and O_2 in air facilitates the complete progression of the wet oxidation reaction. Specifically, in the presence of H_2O and O_2, metastable Si–OC_2H_5 and Si–H groups are converted to Si–OH and further condensed to form stable SiO_x networks, thereby avoiding significant nonradiative recombination caused by the potential degradation of Si–OC_2H_5 and Si–H to dangling bonds ($\equiv$Si·/Si–H $\leftrightarrow$ Si–OC_2H_5 $\rightarrow$ Si–OH $\rightarrow$ SiO_x; $\equiv$Si· $\leftrightarrow$ Si–H $\rightarrow$ Si–OH $\rightarrow$ SiO_x). (2) Most excited and quasi-excited electrons are captured by the four radiative trap states within SiO_x, emitting photons as they transition to the trap ground states. This process significantly reduces the capture of electrons by nonradiative trap states associated with the dangling bonds on the surface of SiQDs.

To evaluate the stability of NUVV-QDs, we stored the freshly prepared sample under ambient conditions (15–25 °C, 30–55% RH) for 54 days, as illustrated in Fig. S8. As shown in Fig. S8(a), the air-stored NUVV-QDs maintained a sky-blue color similar to that of the initial sample under UV light excitation at 365 nm. Fig. S8(b) presents the normalized 2D PL spectra (normalized by the maximum intensity in the 2D spectrum) of both the initial and air-stored samples. The 2D PL spectra of the exposed sample closely resemble those of the initial sample, without any additional defect-induced (NBOHC or STE) or intrinsic emission peaks. This observation indicates that the NUVV emission induced by POLs and ODCs(I) remains the dominant contributor in the air-stored sample. Furthermore, a relative increase in the intensity of the excitation light and a relative decrease in the intensity of the NUVV emission are observed in the air-stored sample. This change reflects a reduction in the absorption capacity of the air-stored sample for the excitation light. This suggests that some of the oxygen-related defects in SiO_x have been passivated, thereby decreasing the density of the radiative trap states. Moreover, the PLQY of the sample decreased from an initial 18.09% to 15.89% after approximately two months of storage in air, further corroborating the previously observed reduction in the density of the radiative trapped states. Previous studies suggest that –Si–O–O–Si– groups exhibit lower stability compared to Si–O–Si,[99,100] leading to a tendency for POLs to decompose into Si–O–Si. Furthermore, ODCs(I) are prone to oxidation by O_2 in air, converting into Si–O–Si. Therefore, the observed decrease in the PLQY without the emergence of new emission peaks can be explained by the partial conversion of POLs and ODCs(I) to Si–O–Si groups. Figs. S8(c) and (d) present the PLE and PL spectra of the samples before and after air storage. Analysis shows that the proportion of the trap state E_{t4} has diminished, confirming the conversion of some POLs to Si–O–Si groups.

Table 3 summarizes the properties of oxide-related SiQDs in the emission range of 300 to 500 nm. The SiQDs produced in this research extend the PL emission peak wavelength of oxide-related SiQDs into the NUVV region, specifically below 400 nm, compared to previously reported SiQDs. Furthermore, these SiQDs exhibit an exceptionally high mean PLQY compared to oxide-related SiQDs reported to date, highlighting the efficacy of this facile wet oxidation treatment.

4. Conclusions

We introduce a facile wet oxidation method to obtain NUVV-emitting SiQDs and reveal their emission mechanism. The prepared NUVV-QDs have an average diameter of 4.95 nm, and their F-band emission peaks, located at 332–420 nm, are blue-shifted by about 500 nm compared to NIR-QDs without wet oxidation treatment. Notably, the average PLQY of the NUVV-QDs is 19.05%, marking a significant 6.24-fold improvement compared to that of the NIR-QDs. Using PL, TEM, XRD, Raman spectroscopy, FTIR, and EPR techniques, we identified two types of oxygen-related defects in SiO_x—POL and ODC(I)—as the origin of the NUVV emission. We propose that the wet oxidation reaction (15–25 °C, 30–55% RH) occurs as follows: (1) the Si–H and dangling bonds are passivated to Si–OC_2H_5 groups by ethanol; (2) the Si–OC_2H_5 groups are hydrolyzed by H_2O in air to form Si–OH groups, while simultaneously, the Si–H bonds are oxidized by O_2 to generate additional Si–OH groups; (3) the produced Si–OH groups condense in large quantities to form SiO_x networks. These networks feature two oxygen-related defects (POL and ODC(I)) rather than simple Si–O–Si groups. In brief, the alkoxylation induced by ethanol serves as the foundation for wet oxidation, while H_2O and O_2 are indispensable for driving the reaction to completion.

The emission mechanism for NUVV-QDs involves four distinct processes: (1) Electrons within the SiQDs absorb UV light, undergoing a direct Γ–Γ transition. (2) A subset of electrons in the CBM of the SiQDs relaxes to nonradiative trap states

Table 3 Properties of SiQDs in the emission range of 300 to 500 nm associated with silicon oxides in recent years

Year	Method	Emission source	Size (nm)	PL peak (nm)	Decay time (ns)	PLQY (%)	Ref.
2010	Co-sputtering	Oxygen-related defects	4.50	420	10	—	73
2011	Plasma	Oxygen-related defects	4.27	450	—	—	74
2011	Laser ablation	Oxygen-related defects	2–10	415–435	—	—	76
2013	HSQ polymer	Siloxane	5.14	488	—	—	75
2015	HSQ polymer	Oxygen-related defects	6.3	450	4.63–15.86	—	40
2022	Reduction of $SiCl_4$	Siloxane	3.0	400	5	12	72
2024	Reduction of $SiBr_4$	SiO_x	5.9	470–480	12	—	77
2024	HSQ polymer	Oxygen-related defects	4.95	332–420	3.73	19.05	This study

introduced by dangling bonds, releasing energy as phonons. Subsequently, they leave these trap states and further relax to the VBM, releasing energy once more in the form of phonons. (3) Most excited or quasi-excited electrons near the CBM of the SiQDs are captured by radiative trap states induced by oxygen-related defects in SiO_x. Similarly, holes at the VBM are captured by the trap ground states introduced by oxygen-related defects. (4) The trapped electrons are released from radiative trap states and transition to the trap ground states, where they recombine with holes, emitting 2.95–3.73 eV of energy in the form of photons. To evaluate the stability of NUVV-QDs, we stored them in ambient air (15–25 °C, 30–55% RH) for approximately two months. For the air-stored sample, neither intrinsic emission nor additional defect-induced emission was observed. Furthermore, the air-stored sample retained 88% of the PLQY of the initial sample. The reduction in the PLQY results from the partial conversion of POLs and ODCs to Si–O–Si groups. These observations indicate that the NUVV-QDs exhibit favorable air stability. This study expands the PL of SiQDs into the NUVV region and seeks to overcome the synthetic challenges associated with the small particle size (<1.53 nm) required for the intrinsic NUVV emission. Additionally, it offers profound insights into the emission mechanisms caused by oxygen-related defects on the surface of SiQDs.

Author contributions

Yizhou He: conceptualization, methodology, formal analysis, investigation, data curation, writing – original and revision draft, and visualization. Qianxi Hao: conceptualization, methodology, investigation, and formal analysis. Chi Zhang: methodology, formal analysis, and data curation. Qi Wang: formal analysis and data curation. Wenxin Zeng: investigation and formal analysis. Jiamin Yu: investigation and resources. Xue Yang: methodology, data curation, writing – review and editing, resources, supervision, and funding acquisition. Shaorong Li: conceptualization, resources, and supervision. Xiaowei Guo: conceptualization, data curation, resources, methodology, writing – review and editing, supervision, and funding acquisition. Serguei K. Lazarouk: review and editing and supervision.

Data availability

The data supporting this article have been included as part of the ESI.†

Conflicts of interest

The authors declare no conflicts of interest.

Acknowledgements

This project was supported by the Sichuan Science and Technology Program (2022ZYD0110) and the China National Tobacco Corporation Sichuan Company (SCYC202120). We would like to thank Dr Yanying, Wang of Analytical & Testing Center Sichuan University for her assistance on steady/transient fluorescence.

References

1 S. Terada, Y. Xin and K.-I. Saitow, *Chem. Mater.*, 2020, **32**, 8382–8392.
2 K.-i Saitow and T. Yamamura, *J. Phys. Chem. C*, 2009, **113**, 8465–8470.
3 S. Wei, T. Yamamura, D. Kajiya and K.-I. Saitow, *J. Phys. Chem. C*, 2012, **116**, 3928–3934.
4 Y. Xin, K. Nishio and K.-I. Saitow, *Appl. Phys. Lett.*, 2015, 106.
5 V. Svrcek, D. Mariotti, U. Cvelbar, G. Filipic, M. Lozac'h, C. McDonald, T. Tayagaki and K. Matsubara, *J. Phys. Chem. C*, 2016, **120**, 18822–18830.
6 Y. Xin, T. Kitasako, M. Maeda and K.-I. Saitow, *Chem. Phys. Lett.*, 2017, **674**, 90–97.
7 A. V. Kabashin, A. Singh, M. T. Swihart, I. N. Zavestovskaya and P. N. Prasad, *ACS Nano*, 2019, **13**, 9841–9867.
8 A. G. Cullis and L. T. Canham, *Nature*, 1991, **353**, 335–338.
9 Y. Kanemitsu, *Phys. Rep.*, 1995, **263**, 1–91.
10 S. Lazarouk, P. Jaguiro, S. Katsouba, G. Maiello, S. La Monica, G. Masini, E. Proverbio and A. Ferrari, *Thin Solid Films*, 1997, **297**, 97–101.
11 J. R. Heath, *Science*, 1992, **258**, 1131–1133.
12 J. Zou, R. K. Baldwin, K. A. Pettigrew and S. M. Kauzlarich, *Nano Lett.*, 2004, **4**, 1181–1186.
13 Q. Li, Y. He, J. Chang, L. Wang, H. Chen, Y.-W. Tan, H. Wang and Z. Shao, *J. Am. Chem. Soc.*, 2013, **135**, 14924–14927.
14 M. Rosso-Vasic, E. Spruijt, B. van Lagen, L. De Cola and H. Zuilhof, *Small*, 2008, **4**, 1835–1841.
15 Q. Li, T.-Y. Luo, M. Zhou, H. Abroshan, J. Huang, H. J. Kim, N. L. Rosi, Z. Shao and R. Jin, *ACS Nano*, 2016, **10**, 8385–8393.
16 Y. Zhong, F. Peng, F. Bao, S. Wang, X. Ji, L. Yang, Y. Su, S.-T. Lee and Y. He, *J. Am. Chem. Soc.*, 2013, **135**, 8350–8356.
17 J. Wang, S. Sun, F. Peng, L. Cao and L. Sun, *Chem. Commun.*, 2011, **47**, 4941–4943.
18 L. Mangolini, E. Thimsen and U. Kortshagen, *Nano Lett.*, 2005, **5**, 655–659.
19 U. R. Kortshagen, R. M. Sankaran, R. N. Pereira, S. L. Girshick, J. J. Wu and E. S. Aydil, *Chem. Rev.*, 2016, **116**, 11061–11127.
20 D. Jurbergs, E. Rogojina, L. Mangolini and U. Kortshagen, *Appl. Phys. Lett.*, 2006, 88.
21 C. M. Hessel, E. J. Henderson and J. G. C. Veinot, *Chem. Mater.*, 2006, **18**, 6139–6146.
22 C. M. Hessel, D. Reid, M. G. Panthani, M. R. Rasch, B. W. Goodfellow, J. Wei, H. Fujii, V. Akhavan and B. A. Korgel, *Chem. Mater.*, 2012, **24**, 393–401.
23 J. R. Rodríguez Núñez, J. A. Kelly, E. J. Henderson and J. G. C. Veinot, *Chem. Mater.*, 2012, **24**, 346–352.
24 M. Dasog, G. B. De Los Reyes, L. V. Titova, F. A. Hegmann and J. G. C. Veinot, *ACS Nano*, 2014, **8**, 9636–9648.

25 Y. Yu, C. E. Rowland, R. D. Schaller and B. A. Korgel, *Langmuir*, 2015, **31**, 6886–6893.
26 M. A. Islam, M. H. Mobarok, R. Sinelnikov, T. K. Purkait and J. G. C. Veinot, *Langmuir*, 2017, **33**, 8766–8773.
27 Y. Yu, G. Fan, A. Fermi, R. Mazzaro, V. Morandi, P. Ceroni, D.-M. Smilgies and B. A. Korgel, *J. Phys. Chem. C*, 2017, **121**, 23240–23248.
28 R. J. Clark, M. Aghajamali, C. M. Gonzalez, L. Hadidi, M. A. Islam, M. Javadi, M. H. Mobarok, T. K. Purkait, C. J. T. Robidillo, R. Sinelnikov, A. N. Thiessen, J. Washington, H. Yu and J. G. C. Veinot, *Chem. Mater.*, 2017, **29**, 80–89.
29 I. Sychugov, A. Fucikova, F. Pevere, Z. Yang, J. G. C. Veinot and J. Linnros, *ACS Photonics*, 2014, **1**, 998–1005.
30 J. Zhou, J. Huang, H. Chen, A. Samanta, J. Linnros, Z. Yang and I. Sychugov, *J. Phys. Chem. Lett.*, 2021, **12**, 8909–8916.
31 A. Marinins, R. Zandi Shafagh, W. van der Wijngaart, T. Haraldsson, J. Linnros, J. G. C. Veinot, S. Popov and I. Sychugov, *ACS Appl. Mater. Interfaces*, 2017, **9**, 30267–30272.
32 G. D. Sorarù, S. Modena, P. Bettotti, G. Das, G. Mariotto and L. Pavesi, *Appl. Phys. Lett.*, 2003, **83**, 749–751.
33 M. J. De Castro and J. C. Pivin, *J. Sol-Gel Sci. Technol.*, 2003, **28**, 37–43.
34 G. Das, L. Ferraioli, P. Bettotti, F. De Angelis, G. Mariotto, L. Pavesi, E. Di Fabrizio and G. D. Soraru, *Thin Solid Films*, 2008, **516**, 6804–6807.
35 E. J. Henderson, J. A. Kelly and J. G. C. Veinot, *Chem. Mater.*, 2009, **21**, 5426–5434.
36 J. A. Kelly, E. J. Henderson and J. G. C. Veinot, *Chem. Commun.*, 2010, **46**, 8704–8718.
37 Y. Xin, R. Wakimoto and K.-I. Saitow, *Chem. Lett.*, 2017, **46**, 699–702.
38 N. Shirahata, J. Nakamura, J.-I. Inoue, B. Ghosh, K. Nemoto, Y. Nemoto, M. Takeguchi, Y. Masuda, M. Tanaka and G. A. Ozin, *Nano Lett.*, 2020, **20**, 1491–1498.
39 M. Miyano, S. Endo, H. Takenouchi, S. Nakamura, Y. Iwabuti, O. Shiino, T. Nakanishi and Y. Hasegawa, *J. Phys. Chem. C*, 2014, **118**, 19778–19784.
40 W. J. I. DeBenedetti, S.-K. Chiu, C. M. Radlinger, R. J. Ellison, B. A. Manhat, J. Z. Zhang, J. Shi and A. M. Goforth, *J. Phys. Chem. C*, 2015, **119**, 9595–9608.
41 B. Ghosh, T. Hamaoka, Y. Nemoto, M. Takeguchi and N. Shirahata, *J. Phys. Chem. C*, 2018, **122**, 6422–6430.
42 M. L. Mastronardi, F. Hennrich, E. J. Henderson, F. Maier-Flaig, C. Blum, J. Reichenbach, U. Lemmer, C. Kübel, D. Wang, M. M. Kappes and G. A. Ozin, *J. Am. Chem. Soc.*, 2011, **133**, 11928–11931.
43 E. J. Henderson, A. J. Shuhendler, P. Prasad, V. Baumann, F. Maier-Flaig, D. O. Faulkner, U. Lemmer, X. Y. Wu and G. A. Ozin, *Small*, 2011, **7**, 2507–2516.
44 S. Chandra, B. Ghosh, G. Beaune, U. Nagarajan, T. Yasui, J. Nakamura, T. Tsuruoka, Y. Baba, N. Shirahata and F. M. Winnik, *Nanoscale*, 2016, **8**, 9009–9019.
45 B. Ghosh, Y. Masuda, Y. Wakayama, Y. Imanaka, J.-I. Inoue, K. Hashi, K. Deguchi, H. Yamada, Y. Sakka, S. Ohki, T. Shimizu and N. Shirahata, *Adv. Funct. Mater.*, 2014, **24**, 7151–7160.
46 H. Yamada, N. Saitoh, B. Ghosh, Y. Masuda, N. Yoshizawa and N. Shirahata, *J. Phys. Chem. C*, 2020, **124**, 23333–23342.
47 J. Watanabe, H. Yamada, H.-T. Sun, T. Moronaga, Y. Ishii and N. Shirahata, *ACS Appl. Nano Mater.*, 2021, **4**, 11651–11660.
48 H. Yamada, J. Watanabe, K. Nemoto, H.-T. Sun and N. Shirahata, *Nanomaterials*, 2022, **12**, 4314.
49 I. T. Cheong, J. Mock, M. Kallergi, E. Groß, A. Meldrum, B. Rieger, M. Becherer and J. G. C. Veinot, *Adv. Opt. Mater.*, 2023, **11**, 2201834.
50 T. M. Atkins, A. Thibert, D. S. Larsen, S. Dey, N. D. Browning and S. M. Kauzlarich, *J. Am. Chem. Soc.*, 2011, **133**, 20664–20667.
51 A. Gupta, M. T. Swihart and H. Wiggers, *Adv. Funct. Mater.*, 2009, **19**, 696–703.
52 S. Terada, H. Ueda, T. Ono and K.-I. Saitow, *ACS Sustainable Chem. Eng.*, 2022, **10**, 1765–1776.
53 K.-Y. Cheng, R. Anthony, U. R. Kortshagen and R. J. Holmes, *Nano Lett.*, 2010, **10**, 1154–1157.
54 D. P. Puzzo, E. J. Henderson, M. G. Helander, Z. Wang, G. A. Ozin and Z. Lu, *Nano Lett.*, 2011, **11**, 1585–1590.
55 K.-Y. Cheng, R. Anthony, U. R. Kortshagen and R. J. Holmes, *Nano Lett.*, 2011, **11**, 1952–1956.
56 L. Yao, T. Yu, L. Ba, H. Meng, X. Fang, Y. Wang, L. Li, X. Rong, S. Wang, X. Wang, G. Ran, X. Pi and G. Qin, *J. Mater. Chem. C*, 2016, **4**, 673–677.
57 X. Liu, S. Zhao, W. Gu, Y. Zhang, X. Qiao, Z. Ni, X. Pi and D. Yang, *ACS Appl. Mater. Interfaces*, 2018, **10**, 5959–5966.
58 H. Ueda and K.-i Saitow, *ACS Appl. Mater. Interfaces*, 2024, **16**, 985–997.
59 Q. He, K. Wang, D. Li, D. Yang and X. Pi, *Adv. Opt. Mater.*, 2024, **12**, 2302422.
60 Z. Ni, L. Ma, S. Du, Y. Xu, M. Yuan, H. Fang, Z. Wang, M. Xu, D. Li, J. Yang, W. Hu, X. Pi and D. Yang, *ACS Nano*, 2017, **11**, 9854–9862.
61 J.-M. Shieh, W.-C. Yu, J. Y. Huang, C.-K. Wang, B.-T. Dai, H.-Y. Jhan, C.-W. Hsu, H.-C. Kuo, F.-L. Yang and C.-L. Pan, *Appl. Phys. Lett.*, 2009, 94.
62 F. Meinardi, S. Ehrenberg, L. Dhamo, F. Carulli, M. Mauri, F. Bruni, R. Simonutti, U. Kortshagen and S. Brovelli, *Nat. Photonics*, 2017, **11**, 177–185.
63 X. Pi, Q. Li, D. Li and D. Yang, *Sol. Energy Mater. Sol. Cells*, 2011, **95**, 2941–2945.
64 S. Zhao, Z. Ni, H. Tan, Y. Wang, H. Jin, T. Nie, M. Xu, X. Pi and D. Yang, *Nano Energy*, 2018, **54**, 383–389.
65 K.-i Saitow, *Bull. Chem. Soc. Jpn.*, 2024, **97**, uoad002.
66 X. Liu, Y. Zhang, T. Yu, X. Qiao, R. Gresback, X. Pi and D. Yang, *Part. Part. Syst. Charact.*, 2016, **33**, 44–52.
67 Z. Ni, S. Zhou, S. Zhao, W. Peng, D. Yang and X. Pi, *Mater. Sci. Eng., R*, 2019, **138**, 85–117.
68 L. Canham, *Faraday Discuss.*, 2020, **222**, 10–81.
69 M. L. Mastronardi, F. Maier-Flaig, D. Faulkner, E. J. Henderson, C. Kübel, U. Lemmer and G. A. Ozin, *Nano Lett.*, 2012, **12**, 337–342.
70 M. Dasog, Z. Yang, S. Regli, T. M. Atkins, A. Faramus, M. P. Singh, E. Muthuswamy, S. M. Kauzlarich, R. D. Tilley and J. G. C. Veinot, *ACS Nano*, 2013, **7**, 2676–2685.

71 M. Dasog, K. Bader and J. G. C. Veinot, *Chem. Mater.*, 2015, **27**, 1153–1156.
72 K. Fujimoto, T. Hayakawa, Y. Xu, N. Jingu and K.-I. Saitow, *ACS Sustainable Chem. Eng.*, 2022, **10**, 14451–14463.
73 W. D. A. M. de Boer, D. Timmerman, K. Dohnalová, I. N. Yassievich, H. Zhang, W. J. Buma and T. Gregorkiewicz, *Nat. Nanotechnol.*, 2010, **5**, 878–884.
74 A. Gupta and H. Wiggers, *Nanotechnology*, 2011, **22**, 055707.
75 S.-K. Chiu, B. A. Manhat, W. J. I. DeBenedetti, A. L. Brown, K. Fichter, T. Vu, M. Eastman, J. Jiao and A. M. Goforth, *J. Mater. Res.*, 2013, **28**, 216–230.
76 S. Yang, W. Li, B. Cao, H. Zeng and W. Cai, *J. Phys. Chem. C*, 2011, **115**, 21056–21062.
77 N. Jingu, K. Sumida, T. Hayakawa, T. Ono and K.-I. Saitow, *Chem. Mater.*, 2024, **36**, 5077–5091.
78 D. F. Swinehart, *J. Chem. Educ.*, 1962, **39**, 333.
79 C. Delerue, G. Allan and M. Lannoo, *Phys. Rev. B: Condens. Matter Mater. Phys.*, 1993, **48**, 11024–11036.
80 B. V. Oliinyk, D. Korytko, V. Lysenko and S. Alekseev, *Chem. Mater.*, 2019, **31**, 7167–7172.
81 G. Wen, X. Zeng, X. Wen and W. Liao, *J. Appl. Phys.*, 2014, 115.
82 S. Lu, B. Wu, Y. Sun, Y. Cheng, F. Liao and M. Shao, *J. Mater. Chem. C*, 2017, **5**, 6713–6717.
83 N. Yao, Y. Zhang, X. Rao, Z. Yang, K. Zheng, K. Świerczek and H. Zhao, *Int. J. Miner., Metall. Mater.*, 2022, **29**, 876–895.
84 T. Ono, Y. Xu, T. Sakata and K.-I. Saitow, *ACS Appl. Mater. Interfaces*, 2022, **14**, 1373–1388.
85 S. Hernández, J. López-Vidrier, L. López-Conesa, D. Hiller, S. Gutsch, J. Ibáñez, S. Estradé, F. Peiró, M. Zacharias and B. Garrido, *J. Appl. Phys.*, 2014, 115.
86 M. Mecozzi and E. Sturchio, *J. Imaging*, 2017, **3**, 11.
87 S. Zafar, A. Ashraf, M. U. Ijaz, S. Muzammil, M. H. Siddique, S. Afzal, R. Andleeb, K. A. Al-Ghanim, F. Al-Misned, Z. Ahmed and S. Mahboob, *J. King Saud Univ., Sci.*, 2020, **32**, 1116–1122.
88 D. Setyaningrum, S. Riyanto and A. Rohman, *Int. Food Res. J.*, 2013, **20**, 1977.
89 K. Dohnalová, T. Gregorkiewicz and K. Kůsová, *J. Phys.: Condens. Matter*, 2014, **26**, 173201.
90 R. Lockwood, Z. Yang, R. Sammynaiken, J. G. C. Veinot and A. Meldrum, *Chem. Mater.*, 2014, **26**, 5467–5474.
91 B. P. Falcão, J. P. Leitão, M. R. Soares, L. Ricardo, H. Águas, R. Martins and R. N. Pereira, *Phys. Rev. Appl.*, 2019, **11**, 024054.
92 H. Ahn, J. Jeong, M. Gu, Y. J. Chang and M. Han, *Optical Materials*, 2024, **147**, 114792.
93 S. Roushdey, in *Crystalline Silicon*, ed. B. Sukumar, IntechOpen, Rijeka, 2011, ch. 8, DOI: 10.5772/22607.
94 R. A. Weeks and C. M. Nelson, *J. Am. Ceram. Soc.*, 1960, **43**, 399–404.
95 H. Song, Z. Li, H. Chen, Z. Jiao, Z. Yu, Y. Jin, Z. Yang, M. Gong and X. Sun, *Appl. Surf. Sci.*, 2008, **254**, 5655–5659.
96 Y. Sakurai, *J. Non-Cryst. Solids*, 2006, **352**, 5391–5398.
97 G. R. Eaton, S. S. Eaton, D. P. Barr and R. T. Weber, *Quantitative Epr*, Springer Science & Business Media, 2010.
98 J. Tang, M. Sakamoto, H. Ohta and K.-I. Saitow, *Nanoscale*, 2020, **12**, 4352–4358.
99 S. Ogawa and N. Shiono, *Phys. Rev. B: Condens. Matter Mater. Phys.*, 1995, **51**, 4218–4230.
100 J. Ushio, T. Maruizumi and K. Kushida-Abdelghafar, *Appl. Phys. Lett.*, 2002, **81**, 1818–1820.

